

A nanocomposite of Au-AgI core/shell dimer as a dual-modality contrast agent for x-ray computed tomography and photoacoustic imaging

Anamaria Orza

Department of Radiology and Imaging Sciences and Center for Systems Imaging, Emory University School of Medicine, Atlanta, Georgia 30322

Yi Yang

Department of Radiology and Imaging Sciences, Emory University School of Medicine, Atlanta, Georgia 30322

Ting Feng and Xueding Wang

Department of Biomedical Engineering, University of Michigan School of Medicine, Ann Arbor, Michigan 48109

Hui Wu and Yuancheng Li

Department of Radiology and Imaging Sciences and Center for Systems Imaging, Emory University School of Medicine, Atlanta, Georgia 30322

Lily Yang

Department of Surgery, Emory University School of Medicine, Atlanta, Georgia 30322

Xiangyang Tang^{a)}

Department of Radiology and Imaging Sciences, Emory University School of Medicine, Atlanta, Georgia 30322

Hui Mao^{a)}

Department of Radiology and Imaging Sciences and Center for Systems Imaging, Emory University School of Medicine, Atlanta, Georgia 30322

(Received 13 August 2015; revised 29 October 2015; accepted for publication 12 December 2015; published 7 January 2016)

Purpose: To develop a core/shell nanodimer of gold (core) and silver iodine (shell) as a dual-modal contrast-enhancing agent for biomarker targeted x-ray computed tomography (CT) and photoacoustic imaging (PAI) applications.

Methods: The gold and silver iodine core/shell nanodimer (Au/AgICSD) was prepared by fusing together components of gold, silver, and iodine. The physicochemical properties of Au/AgICSD were then characterized using different optical and imaging techniques (e.g., HR- transmission electron microscope, scanning transmission electron microscope, x-ray photoelectron spectroscopy, energy-dispersive x-ray spectroscopy, Z-potential, and UV-vis). The CT and PAI contrast-enhancing effects were tested and then compared with a clinically used CT contrast agent and Au nanoparticles. To confer biocompatibility and the capability for efficient biomarker targeting, the surface of the Au/AgICSD nanodimer was modified with the amphiphilic diblock polymer and then functionalized with transferrin for targeting transferrin receptor that is overexpressed in various cancer cells. Cytotoxicity of the prepared Au/AgICSD nanodimer was also tested with both normal and cancer cell lines.

Results: The characterizations of prepared Au/AgI core/shell nanostructure confirmed the formation of Au/AgICSD nanodimers. Au/AgICSD nanodimer is stable in physiological conditions for *in vivo* applications. Au/AgICSD nanodimer exhibited higher contrast enhancement in both CT and PAI for dual-modality imaging. Moreover, transferrin functionalized Au/AgICSD nanodimer showed specific binding to the tumor cells that have a high level of expression of the transferrin receptor.

Conclusions: The developed Au/AgICSD nanodimer can be used as a potential biomarker targeted dual-modal contrast agent for both or combined CT and PAI molecular imaging. © 2016 American Association of Physicists in Medicine. [<http://dx.doi.org/10.1118/1.4939062>]

Key words: contrast agent, core-shell, computer tomography, gold, silver iodine, nanoparticles, photoacoustic imaging

1. INTRODUCTION

Diagnostic imaging and imaging assisted interventions play important roles in clinical care and in the research and development of precision medicine, a customized form of health-

care designed to address specific patient concerns. Currently, various imaging modalities, such as x-ray computed tomography (CT), magnetic resonance imaging (MRI), position emission tomography (PET), and single photon emission computed tomography (SPECT), are already available in

clinical practices.¹ Each of these imaging modalities offers specific capabilities and functions with their strengths and limitations related to the contrast mechanism associated to the specific tissue and physiological conditions, sensitivity and specificity to a disease specific measurement, the spatial and anatomic coverage of organs, and the cost effectiveness when applied to a specific diagnosis. To take advantage of synergies while also reconciling the various limitations of each individual modality, multimodal imaging approaches and systems are of great interest for preclinical research and clinical practices. By integrating multiple imaging techniques with compatible and complementary contrast agents, multimodal imaging may offer several benefits, such as providing complementary diagnostic information given by the strengths of each modality, reducing image acquisition and processing time, and lowering the exposure risk with a one-time administration of the multimodal and multifunctional contrast agent.²⁻⁴ Therefore, there is an emerging need in developing novel multimodal and multifunctional contrast materials and molecular imaging probes for multimodal imaging applications. To date, a number of integrated imaging modalities have been developed, including MRI/optical,⁵ MRI/PET,⁶ PET/near-infrared (NIR) optical fluorescence^{7,8} CT/MRI,⁹ CT/photoacoustic imaging (PAI),¹⁰ and SPECT/CT.^{11,12}

Nanomaterials are particularly suited for developing novel dual-modal imaging contrast agents, either with single composition¹³⁻¹⁶ or with hybrid of multiple components.¹⁷⁻²⁰ The latter has been shown for the enhanced properties for imaging and therapeutics. Specifically, new nanoparticle based contrast agents combining CT and PAI capabilities provide fine anatomic details with CT and physiological or targeted imaging with PAI for accurate detection and localization of pathological lesions.²¹⁻²³ For instance, Tian *et al.*²² recently reported that Rb-TB can be employed as a new dual-modal contrast agent for CT and PAI imaging because of its high NIR optical absorption capability and strong x-ray attenuation ability. Another study using Bi₂S₃@SiO₂ nanorods as a CT and PAT dual-modal contrast agent demonstrated a real-time noninvasive visualization of nanorods distribution in the gastrointestinal tract.²³

Therefore, dual-modal contrast agents with well-controlled structural, physical characteristics (i.e., size, and shell thickness, shape, optical, thermal, MR relaxivities, and acoustic) and high stability and functions in the physiological conditions are highly desired, since, these agents lead to a better understanding of real-time biological processes in a variety of physiological or pathological conditions. Herein, we report the development of a new class of CT-PAI dual-modal contrast agents that are composed by a core/shell nanodimer of fused gold and silver iodine (Au/AgICSD) coated with amphiphilic PEG-*b*-AGE polymer and functionalized with CALNN peptides that can be used for conjugating biomarker targeting moieties. The developed Au/AgICSD nanodimer shows efficient contrast enhancement in both CT and PAI and capability of targeted imaging of cancer cells with transferrin receptor (TfR) overexpression, demonstrating the potential to facilitate targeted diagnosis and therapy with integrated CT and PAI techniques.

2. MATERIALS AND METHODS

2.A. Materials

Hydrogen tetrachloroaurate(III) trihydrate (HAuCl₄·3H₂O), trisodium citrate (HOC(COONa)(CH₂COONa)₂·2H₂O) silver nitrate (AgNO₃), ascorbic acid (C₆H₈O₆), CTAC((C₁₆H₃₃)N(CH₃)₃Cl), and sodium iodide (NaI) were purchased from Fisher chemicals. CALNN anchoring group was ordered from California Peptide (San Diego, CA, USA). Transferrin, dimethylthiazol-2-yl-2,5-diphenyltetrazolium bromide (MTT), the PD-10 desalting columns, and the FluoroTag™ FITC conjugation kit were purchased from Sigma-Aldrich. All cell culture materials (media and supplements) were purchased from Invitrogen (Burlington, OH). The Omnipaque™ 350 was purchased from Medline (Waukegan, IL). All chemicals were used without further purification.

2.B. Methods

2.B.1. Preparation of the colloidal gold nanoparticles (AuNPs)

Briefly, 0.03 g of HAuCl₄·3H₂O was dissolved in 300 ml of water and heated to near boiling temperature. Aqueous trisodium citrate solution (9 ml, 0.034 M, ca. 60 °C) was added into the solution. The mixture was refluxed for 40 min and then allowed to cool to room temperature. The resulting ruby red solution was stirred overnight and then finally filtered (0.45 μm, Millipore filter) to collect AuNPs. Obtained AuNPs were characterized by UV-vis spectroscopy, giving the typical plasmon band at 520 nm. The as-prepared AuNPs were concentrated by centrifugation and used as seeds for the ensuing reaction for making the designed core-shell nanocomposites.

2.B.2. Preparation of the Au/AgICSD

The synthesized AuNPs were used as seeds while a mixture of AgNO₃ (2 mM) and KI (2 mM) was used as the precursor for growing nuclei. The nucleation and growth kinetics of the shells were manipulated. Briefly, an aqueous solution of ascorbic acid (2 ml, 2 mM) was added into the solution with AuNP seeds (5 ml, 185 nM). The resulted mixture was gently stirred and heated to 60 °C for 15 min. Silver nitrate (4 ml, 2 mM) and KI (4 ml, 2 mM) were then added drop-wise into the reaction mixture at a rate flow of 0.75 ml/min. The resulting Au/AgICSD (a core diameter of 15 nm and a 4 nm thick shell) was subjected to centrifugation (9000 rpm for 40 min) to remove excess reagents and redispersed in 50 ml water. An aqueous solution of citrate (5 ml, 100 mM) was added into redispersed Au/AgICSD nanodimers and mixed overnight.

2.B.3. Preparation of PEG-*b*-AGE coated Au/AgICSD

In order to apply a coating layer on Au/AgICSD nanodimers for surface stabilization and functionalization, the obtained core/shell nanodimers were transferred to THF solution using thiolated styrene. Then, the polyethylene glycol and

polyallyl glycidyl ether blocked co-copolymer (PEG-*b*-AGE), synthesized as we previously reported, was applied to replace the hydrophobic styrene molecules from the Au/AgICSD surface. Briefly, Au/AgICSD nanodimers (10 mg) were dispersed in THF (2 ml) and added drop-wise to the PEG-*b*-AGE solution in THF (18 ml, 5 mg/ml), stirred for 24 h at room temperature. The resulted mixture was then added drop-wise to 200 ml DI water. This aqueous mixture was dialyzed against water for 48 h to remove the excess THF and the unreacted polymer, and then was further centrifuged at 3000 rpm for 5 min. The resulted supernatant of AgI/AuICSD nanodimers was coated by PEG-*b*-AGE grafted with $-NH_2$ groups available for further conjugation of selected targeting ligands.

2.B.4. Preparation of TfR targeted Au/AgICSD (Tf-Au/AgICSD)

The PEG-*b*-AGE coated Au/AgICSD nanodimers were dissolved in PBS at the final concentration of 2 mg/ml and then were incubated with a CALNN peptide linker at molar ratio of 1:4000 for 1 h. The resulting solution was purified on a PD-10 column and CALNN conjugated Au/AgICSD nanodimers were obtained. On the other hand, Tf was mixed with Traut's reagent (in the molar ratio of 1:15) in 0.1M borate buffer, pH 8.5, and incubated overnight at room temperature. The solution mixture was then purified with a desalting spin column to remove the excess of Traut's reagent and obtain the pure thiolated transferrin moieties (Tf-SH). In the final step, the CALNN functionalized Au/AgICSD nanodimers and Tf-SH were incubated at room temperature for 4 h. Tf-Au/AgICSD nanodimers were separated from the solution using a PD-10 desalting column. The process was repeated three times and was performed at 4 °C. The estimation of transferrin moieties conjugated on the surface of Au/AgICSD nanodimers was determined using a BCA protein assay and the concentration of gold was determined by spectroscopy methods. The molar extinction coefficient used to determine their concentration was $\epsilon = 3.67 \times 10^8$. It should be noted that in all the experiments Tf molecules used were also labeled with fluorescent dye FITC based on the vender (Sigma-Aldrich) provided protocol.

2.B.5. Electron microscope and spectroscopic characterizations of Au/AgICSD

Both the size and morphology of the synthesized nanodimers were assessed using a transmission electron microscope (TEM, HitachiH-7500 accelerating voltage 75 kV) energy-dispersive x-ray spectroscopy (EDX). Scanning transmission electron microscope (STEM) measurements were performed with a FEI Tecnai G2 F30 super-twin transmission electron microscope operating at 300 kV. The samples were prepared by dropping a diluted amount of nanoparticles onto the carbon coated grid to air-dry. The UV-vis absorption spectra were obtained using a Shimadzu UV-2401PC UV-visible spectrophotometer with a slit width of 1.0 nm. The elemental composition of the synthesized nanoparticles was assessed by using x-ray photoelectron spectroscopy (XPS) with argon-ion etching. The qualitative and quantitative

analyses of the nanodimers were performed using a SPECS custom-built system. Excitation was produced using the aluminum anode of the x-ray source ($h\nu = 1486.6$ eV). In addition, the surface charge and the hydrodynamic size were measured by using a dynamic light scattering (DLS) instrument (Malvern Zeta Sizer Nano S-90) equipped with a 22 mW He-Ne laser operating at 632.8 nm.

Inductively coupled plasma mass spectroscopy (ICP-MS) was employed to quantitatively measure the composition of each element of the Au/AgICSD core-shell nanodimers. The ICP-MS measurements were carried out with a quadrupole ICP-MS instrument (Elan DRC-e, PerkinElmer, Germany), equipped with a cross flow nebulizer and a Scott double pass spray chamber. Indium is used as an internal standard. Before analysis of the torch position, RF power, nebulizer gas flow, and lens voltage are carefully optimized. Standard Au nanoparticles (AuNPs) were used as a reference material for all analyses.

Statistical analyses for mean value, standard deviation, and Student's *t*-test of the measurements were performed using Microsoft Office Excel software (Microsoft Corporation, Redmond, WA, USA).

2.B.6. Cytotoxicity evaluation

Cytotoxicity of the nanoparticles was examined using 3-(4,5-dimethylthiazol-2-yl)-2,5-phenyltetrazolium bromide (MTT) assay with four different cell lines, i.e., HEK293 human embryonic kidney cell, HeLa human cervical carcinoma cell, MDA-MB-231 human breast cancer cell, and D556 human brain tumor medulloblastoma cell. The cells were maintained as an adherent culture and grown as a monolayer in a humidified incubator (95% air, 5% CO₂) at 37 °C in a cell culture flask containing medium supplemented with 1% penicillin-streptomycin and 10% FBS. Cells were detached and seeded in 96-well flat-bottom microplates at 4000 cells per well. After 24 h recovery at 37 °C, the medium was replaced with 100 μ l medium containing nanoparticles (Au/AgICSD or AuNPs) at various gold concentrations (12.5–400 μ g/ml). For the control cell sample, a fresh medium without nanoparticles was added. After 24 h of incubation at 37 °C, 10 μ l of MTT solution (5 mg/ml) was added into each well following a 4 h incubation period. After removing the culture media, the precipitated formazan was then dissolved in 10% SDS in 0.01M HCl. Finally, a microplate reader (Biotech Synergy2) was used to measure the absorption of all samples ($n = 6$ per group) at 570 nm. Cell viability was determined by comparing the absorptions of cells incubated with and those without nanoparticles.

2.B.7. Targeting and specific cell binding of Au/AgICSD to cells with TfR over expression

D556 medulloblastoma cell lines with a high level of TfR overexpression were used for testing the specificity of Tf-Au/AgICSD. Cells treated with Tf-Au/AgICSD were labeled with FITC at 37 °C for 3 h. Au/AgICSD conjugated with BSA (BSA-Au/AgICSD) was prepared as a control for nontargeted

agent. Briefly, cells were maintained as an adherent culture and grown as a monolayer in a humidified incubator (95% air, 5% CO₂) at 37 °C in a cell culture dish containing medium supplemented with 1% penicillin-streptomycin and 10% FBS. Cells were then seeded in eight-well chambered slides at the concentration of 50 000 cells per well. After 36 h of incubation, the media were replaced and the nanoparticles were added into the cell media at a final concentration of 5 nM and further incubated at 37 °C for 3 h. The cell media were then discharged and the cells were washed three times with PBS. The cell internalization of the targeted nanoparticles was observed using a Zeiss (Germany) fluorescent microscope with an excitation at wavelength 488 nm and emission at wavelength 515 nm.

2.B.8. Evaluation of the contrast effect for computed tomography imaging

Solutions of Au/AgICSD with gold concentrations varying from 0.5×10^3 , 2.5×10^3 , 12.6×10^3 , 17.7×10^3 , 25×10^3 , and 50×10^3 nM were added into PCR tubes as imaging phantoms for the investigating contrast-enhancing effect. The contrast phantoms with distilled water as background were scanned at a peak voltage of 45 keV using a micro-CT consisting of a microfocus (12 μ m) x-ray tube and a flat panel x-ray detector at $48 \times 48 \mu\text{m}^2$ detector cell size. AuNPs at similar Au concentrations with Au/AgICSD and a clinically used iodine contrast agent, Omnipaque 350, at different iodine concentrations of 4.2×10^3 and 9.7×10^3 nM are included as controls. After a 4×4 binning in projection data, tomographic images of the samples were reconstructed at $0.192 \times 0.192 \text{ mm}^2$ pixel size, corresponding to a spatial resolution of 2.6 lp/mm. Hounsfield unit (HU) values of each sample were measured and compared. The CT contrast (i.e., CT number in HU) of each Au/AgICSD solution, is defined as $\text{Contrast} = \text{Mean}_{\text{Target}} - \text{Mean}_{\text{Background}}$, where $\text{Mean}_{\text{Target}}$ and $\text{Mean}_{\text{Background}}$ are the average CT numbers gauged in the region of interest (ROI) placed in the target and background (water) areas, respectively.

2.B.9. Measurement of photoacoustic (PA) signals

To test the capability of prepared nanocomposites for PAI, we measured the photoacoustic signals of each sample using a home-built PAI instrument. A Q-switched Nd:YAG laser was adopted to provide 532-nm laser pulses with a full-width half-

maximum (FWHM) value of 6.5 ns. An OPO system (Vibrant B, Oportek) pumped by the second harmonic of a Nd:YAG laser (Brilliant B, Bigsky) was used to provide laser pulses with a repetition rate of 10 Hz and a pulse width of 5.5 ns. The wavelength for PA measurement in this study was 532 nm, which was determined as an optical absorption wavelength for both Au/AgICSD nanodimers and AuNPs according to results from UV spectra of those nanoparticles. During the PA measurement, each sample was placed in a glass tube (2 mm in diameter) to avoid the variations that may be induced by the illumination of strong laser on the sample, e.g., laser induced temperature rise or change in optical absorption. The laser beam, 2 mm in diameter, illuminates the sample surface and generates PA signals which can be collected by a 10 MHz focused transducer (V312, Panametrics). The sample and the transducer were immersed in water for acoustic coupling. The PA signals from the samples were recorded by a digital oscilloscope (TDS 540B, Tektronics). To compare the performance of Au/AgICSD and AuNPs, PA signals from Au/AgICSD and AuNPs samples at different concentrations were measured at intervals of 20, 10, and 7 nM, and at an interval concentration that provided for a signal-to-noise ratio (SNR) of 2.

3. RESULTS

3.A. Synthesis and characterization of Au/AgICSD

The schematic illustration of the major steps used for the production of Au/AgICSD nanodimer is shown in Fig. 1. Highly monodispersed citrate coated AuNPs with an averaged core diameter of 15 nm were first synthesized and then utilized as seeds for the growth of the shells. In order to initiate the nucleation of shells, ascorbic acid was used as a reduction agent and the iodine and silver shells were reduced on the seed surface. The resulted core-shell nanodimers were further decorated with PEG-*b*-AGE and CALNN anchoring peptide.

To confirm and demonstrate the formation of the core/shell structure along with the composition of the nanodimers, shell coverage, and their surface protection, spectroscopic and electron microscopic imaging characterizations of Au/AgICSD were performed using TEM, STEM, XPS, and ICP-MS. TEM images [Figs. 2(A) and 2(C)] show the high and bright contrast of the Au core compared with the AgI shell which confirms the formation of the multicomponent nanoparticles.

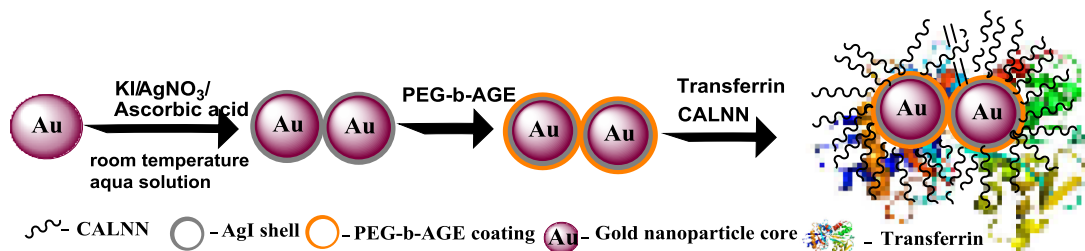


FIG. 1. Schematic illustration of the major steps used for the production of Au/AgICSD, their functionalization with transferrin through the CALNN anchoring groups, and with the surface preserve PEG moieties.

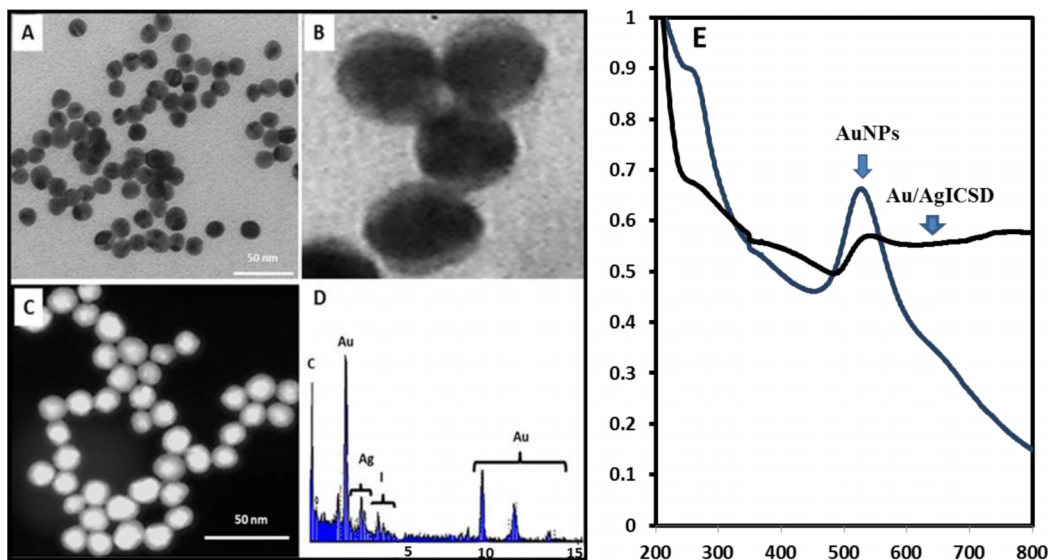


FIG. 2. TEM images of (A) Au/AgICSD nanocomposites, (B) a magnified image of Au/AgICSD nanodimers, (C) STEM image of Au/AgICSD nanodimers, (D) EDS data of Au/AgICSD nanodimers and, (E) UV-vis spectra of gold nanoparticles (blue line) and Au/AgICSD nanocomposites (black line).

Furthermore, TEM revealed that the AgI shell (with a thickness of 5 nm) covers the internal Au core and mediated the formation of the dimers. The composition of the Au/AgICSD components was performed by ICP-MS analysis of Au, Ag, and iodine [Fig. 2(D)]. The fractions of each metal component in Au/AgICSD were 1001.2 ppm for Au, 184.9 ppm for Ag, and 1433.9 ppm for iodine as revealed by ICP-MS. Interestingly, optical properties of Au/AgICSD as shown in Fig. 2(D) are attributed to the anisotropic and dimer-like shape of Au/AgICSD nanocomposite. The absorption curves reveal two peaks associated to the gold nanoparticles composition (at

532 and 760 nm), corresponding to the longitudinal plasmon excitation at 530 nm and transversal plasmon excitation at 760 nm, respectively. In addition, one peak for the silver shell appears at 420 nm and the iodine composition appears around 280 nm.

To confirm the core-shell structure observed in TEM, XPS was performed on Au/AgICSD nanocomposites. Figure 3 shows the XPS narrow scan for Au 4*f*, Ag 3*d*, I 3*d*, and C1 of the Au/AgICSD (survey scan in the supplementary material²⁴). The presence of each element was determined by its corresponding binding energy (BE).

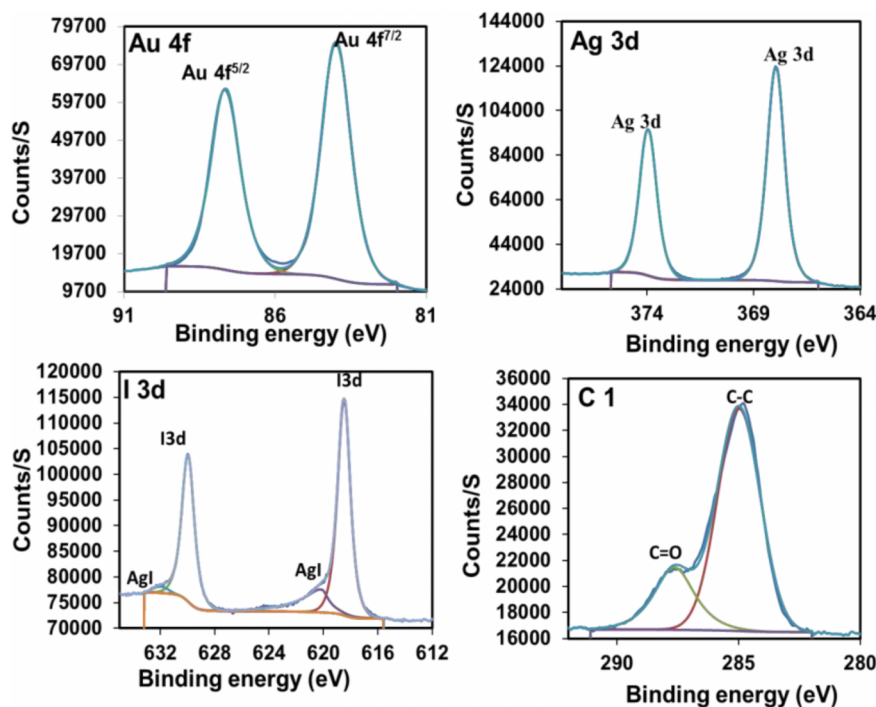


FIG. 3. Binding energy profiles of Au 4*f*, Ag 3*d*, I 3*d*, and C1 for the Au/AgICSD nanocomposites obtained from the XPS narrow scan, top left panel: Au 4*f* (5/2 and 7/2), top right panel: Ag 3*d* (5/2 and 7/2), bottom left: I 3*d* (5/2 and 7/2), bottom right: C1 scans.

The Au-4*f*, Ag-3*d*, and I-3*d* signals from XPS spectra of Au/AgICSD revealed several spin orbit pairs. Their BE values are assigned as follows: 83.8 and 87.7 eV for Au-4*f* (7/2, 5/2), 367.8 and 374.0 eV for Ag-3*d* (7/2, 5/2), and 618.2.0 and 630.2 eV for I-3*d* (7/2, 5/2). The presence of two small additional AgI peaks confirms the observation of the tridomain nanodimer peaks that appear in the iodine scanning. These two peaks are assigned at 621.0 and 632.0 eV, respectively. Moreover, two components in the C-1*s* spectra were resolved using the peak fitting, such as C—C bonds at 285.0 eV and for C=O at 285.5 eV corresponding to the organic molecules.

The stability and surface functions of Au/AgICSD were obtained by coating with the PEG-*b*-AGE copolymer previously reported by our group.²⁵ Since the surface coating procedure needs to be performed in a nonaqueous inorganic/organic solvent, a styrene linker was first applied to the Au/AgICSD nanoparticles. Further, an exchange between styrene coating molecules and PEG-*b*-AGE polymer was performed by stirring them at room temperature for 24 h. The resulted solution was dialyzed against water to obtain PEG-*b*-AGE-Au/AgICSD nanodimers. The average thickness of the polymer coating is approximately 2 nm and the final Au/AgICSD nanodimer is about 37 nm with a polydispersity index (PDI) of 0.254.

3.B. Conjugation of transferrin to Au/AgICSD (Tf-Au/AgICSD)

The successful grafting of the Tf on the surface of the nanodimers was first confirmed by XPS analysis (Fig. 4), in which a new C=C *sp*³ covalent bond is formed while the

C—C *sp*² from Tf and the C—N bond from both CALNN and Tf disappear.

Z-potential measurement also confirms the transferrin functionalization as demonstrated by the Z-potential value changing from 23 mV for PEG-*b*-AGE coated Au/AgICSD with —NH₂ groups on the surface to —35 mV for Tf-Au/AgICSD after the transferrin grafting (Fig. 4, bottom right panel).

3.C. Target specific binding and cytotoxicity of Tf-Au/AgICSD

3.C.1. Targeting capability

The targeting capability of developed Tf-Au/AgICSD was tested *in vitro* using D556 medulloblastoma cells with TfR over expression. Cells were incubated with both targeted, Tf-Au/AgICSD conjugated with FITC labeled Tf and nontargeted Au/AgICSD conjugated with FITC labeled BSA (BSA-Au/AgICSD) as a control. Furthermore, we also used a blocking experiment to confirm the binding specificity of the targeted Tf-Au/AgICSD in which a fixed amount of Tf was incubated with the cells to block the transferrin receptors before adding the nanoparticles. Fluorescence images in Figs. 5(A)–5(D) show that the green fluorescence from FITC is stronger in cells treated with Tf-Au/AgICSD [Fig. 5(B)] compared to the cells treated with BSA-Au/AgICSD [Fig. 5(C)]. The blocking of transferrin receptors reduced the cell uptake of targeted Tf-Au/AgICSD [Fig. 5(D)]. These results indicate that the specific uptake of the Tf-Au/AgICSD into the cancerous cells (that express high levels of TfR) is likely via a receptor-mediated

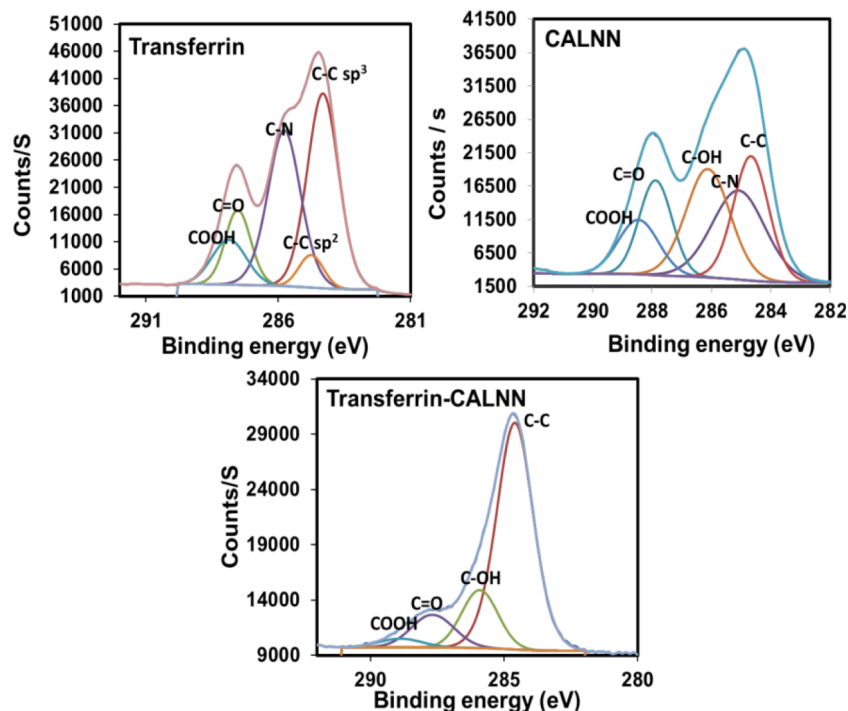


FIG. 4. Binding energy profiles of different samples obtained from C1 XPS narrow scans. Transferrin (top left panel), CALNN (top right panel), Tf-Au/AgICSD nanodimer nanoparticles (bottom panel).

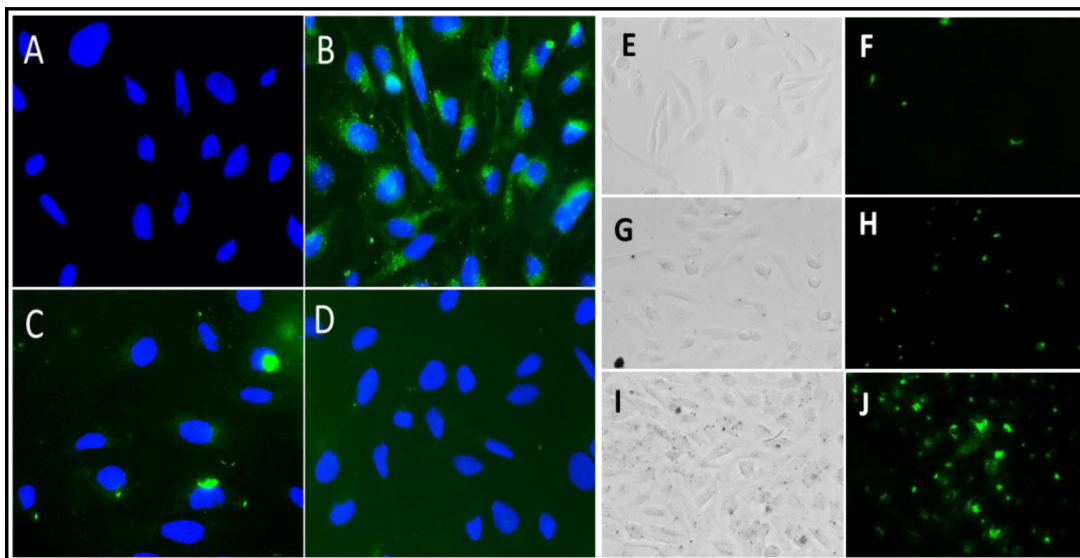


FIG. 5. [(A)–(D)] Fluorescence images of the D556 medulloblastoma cells treated with different nanocomposites: control cells (A), cells treated with Tf-Au/AgICSD (B), cells treated with BSA-Au/AgICSD (C), cells pretreated with a fix amount of Tf before adding the Tf-Au/AgICSD (D). Magnification is 40 \times . Tf and BSA were labeled with FITC.

pathway. Furthermore, in order to demonstrate the uptake of the Tf-AgI/-AuCSD into the cancer cells via receptor-mediated internalization, fluorescence cell imaging was performed with Tf-Au/AgICSD treated D556 medulloblastoma cancer cells at different time points. The green fluorescence images show a time dependent internalization of the FITC labeled Tf-AgI/-AuCSD into the D556 cancerous cells after 30 min [Fig. 5(E) and 5(F)], 1 h [Figs. 5(G) and 5(H)], and 3 h [Figs. 5(I) and 5(J)] incubation. A weak green fluorescence signal from cell internalized nanoparticles was observed in the cells after 30 min of incubation with FITC labeled Tf-Au/AgICSD.

In comparison, green fluorescence of FITC labeled Tf-Au/AgICSD treated cells became much stronger after 3 h of incubation. This observation is consistent with the early study by Yang *et al.*²⁶ which reported that the transferrin conjugated gold nanoparticles were internalized by cells through the endocytosis pathways shown in their atomic force microscopy imaging.

3.C.2. Cytotoxicity evaluation

The toxicity of citrate coated AuNPs and AgI-AuCSD as well as amphiphilic PEG-*b*-AGE polymer coated AuNPs and AgI/AuCSD was evaluated at different concentrations (range from 12.5 to 400 $\mu\text{g}/\text{ml}$) using MTT assay with four types of cells: MDA231 breast cancer cells, human embryonic kidney 293 cells, HeLa cells, and D556 medulloblastoma cells. The MTT experiments were done with 24 and 48 h, respectively. The results normalized to that of Au nanoparticles (stabilized with citrate) are presented in the supplementary material [1(A)–1(D)].²⁷ All nanoparticles tested presented some degrees of acute toxicity under the conditions used in the study. However, the citrate-stabilized AgI-AuCSD exhibited less cytotoxicity on the MDA 231

breast cancer cell line compared to other nanoparticles after 48 h of exposure. Moreover, coating the nanoparticles with copolymer (PEG-*b*-AGE) improved the biocompatibility of the nanomaterials [Figs. 6(A)–6(D)]. The synthesized PEG-*b*-AGE coated Au/AgICSD did not show any significant toxicity up to 50 $\mu\text{g}/\text{ml}$.

3.D. X-ray attenuation properties of Au/AgICSD in CT imaging

The CT images corresponding to the contrast agent are presented in Fig. 7(A), with their corresponding intensities in Hounsfield units that were measured using the method specified in Sec. 2.B.8. Compared with the clinically used iodine agent, Omnipaque 350, both Au/AgICSD and AuNPs showed enhanced contrast in CT, though, Au/AgICSD exhibited significantly stronger contrast. The HU values of the samples with different amounts of gold in nM were obtained and presented in Fig. 7(A) such as for AuNPs: 0.5×10^3 nM—4.2 HU [Fig. 7(a)]; 2.5×10^3 nM—11.7 HU [Fig. 7(b)]; 12.6×10^3 nM—62.3 HU [Fig. 7(c)]; 17.7×10^3 nM—86.8 HU [Fig. 7(d)]; 25×10^3 nM—98.4 HU [Fig. 7(e)]; 50×10^3 nM—266 HU [Fig. 7(f)]; for AgI/AuCSD: 0.5×10^3 nM—79.8 HU [Fig. 7(h)]; 2.5×10^3 nM—136.0 HU [Fig. 7(i)]; 12.6×10^3 nM—230.1 HU [Fig. 7(j)]; 17.7×10^3 nM—376 HU [Fig. 7(k)]; 25×10^3 nM—558.9 HU [Fig. 7(l)]; 50×10^3 nM—1240.8 HU [Fig. 7(m)]; for clinically used Omnipaque 350 iodine contrast capability: 4.2×10^3 nM—134.4 HU [Fig. 7(g)] and 9.7×10^3 nM—195.9 HU [Fig. 7(n)]. HU intensity corresponding to the contrast agents increases proportionally with the concentration [Fig. 7(B)].

The concentrations were determined by ICP-MS. It is found that adding a AgI shell on Au/AgICSD generates substantially stronger contrast than the AuNP core in CT images, suggesting that the loading of iodine in the shell of gold nanoparticles is

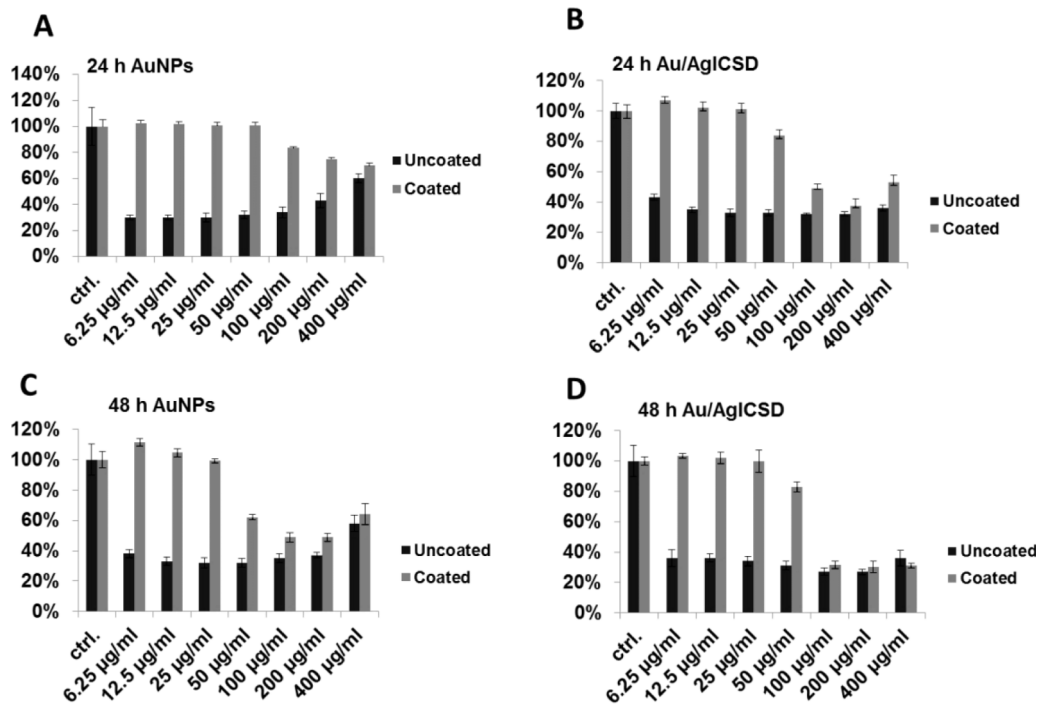


FIG. 6. [(A)–(D)] *In vitro* toxicity investigations of different concentrations of PEG-*b*-AGE and citrate coated AuNPs and Au/AgICSD (at different concentrations 12.5–400 µg/ml) on D556 medulloblastoma cells, incubation time 24 and 48 h.

an efficient method to enhance the contrast without the need of increasing the amount of gold.

3.E. Characterization of Au/AgICSD in PA measurements

The results of photoacoustic measurements and the quantification of the peak to peak value of both Au/AgICSD and AuNP samples at different concentrations are shown in

Fig. 8. The photoacoustic signal from Au/AgICSD is much higher than that from AuNPs at the same concentrations. The concentrations leading to photoacoustic measurement of SNR of 2 were 3 and 0.2 nM, respectively, for AuNPs and Au/AgICSD. Therefore, the ratio between the molar extinction coefficients of Au/AgICSD and AuNPs is about 15, again suggesting that the loading of iodine in the shell of gold nanoparticles may contribute to the increase of the optical absorption contrast of the Au/AgICSD over pure AuNPs.

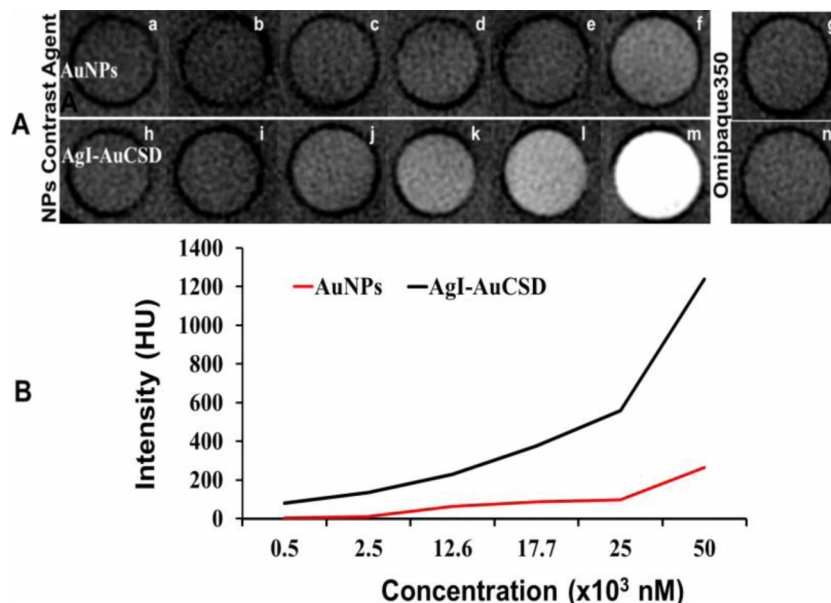


FIG. 7. X-ray CT images of solution phantoms of different materials. (A) Au/AgICSD and AuNPs (used as a control) prepared in a serial of dilutions along with clinical iodine contrast agent Omipaque 350 dilution. (B) The nanoparticulate diluted samples and their corresponding HU value.

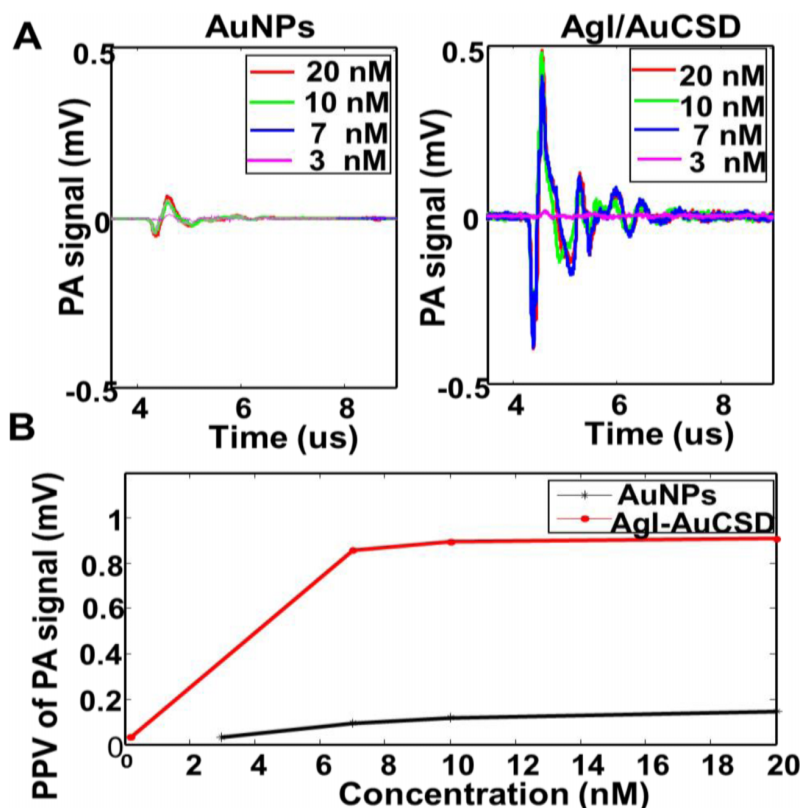


Fig. 8. (A) PA signals from Au/AgICSD and AuNPs samples at different concentrations calibrated based on the amount of Au in the samples. (B) PPV of photoacoustic signals from Au/AgICSD and AuNPs samples corresponding to different concentrations.

4. DISCUSSION

We demonstrated that nanodimers of AgI/Au core-shell nanocomposites can be prepared by using a novel seed mediated approach, in which AuNPs are used as seeds for the core and the composite shell of AgI then can be deposited and assembled on the core spontaneously from solutions of silver nitrate and potassium iodine. The layers of the AgI shell of two core/shell particles then undergo fusion based on the nonepitaxial shell growth, resulting in the formation of a nanodimer. The formation and growth of the dimer structure is likely due to the spontaneous chemisorption of iodine on the surface of aspartic acid AuNPs. The rapid chemisorption of iodine on gold was observed by Cheng *et al.*²⁸ previously. They demonstrated that the chemisorption of iodine takes place on the citrate-stabilized gold nanoparticles in a controllable manner, due to the electron donation between the KI and citrate molecules, thus promoting the fusion of gold nanoparticles together. The mechanism responsible for the formation of Au/AgICSD dimer is believed to be similar to Ostwald ripening (i.e., the small crystals of the sol solutions are depositing on the surfaces of the seed particles), where the KI addition enhances the rate of the Ostwald ripening process. Moreover, Shipway *et al.* have reported that the interactions between iodine and gold are very strong.^{29,30} Additionally, XPS peak values for the binding energy (Fig. 3) are shifted to the lower energy area compared with their corresponding pure metals reported in the literature.^{31,32} This peak shifting

suggests the interaction of the shell with the Au core surface, and it might be explained by a decreased electron density on the interacting metal atoms or that the metal atoms are in an oxidized state as they are coupling with the shell. This decrease of the binding energy in the XPS spectra appears to be inconsistent with some previous reports.^{33,34} Moreover, the presence of two small additional AgI peaks confirms the observation of the tridomain nanodimer peaks that appear in the iodine scanning. These two peaks are assigned at 621.0 and 632.0 eV, respectively.

We showed that functionalization of the Au/AgICSD with the cell targeting moiety transferrin can be accomplished Au/AgICSD through a CALLN linker attached to PEG-*b*-AGE polymer coated on the nanoparticle surface via the amide bond formation between the NH₂ groups of the polymer and COOH group of CALNN linker. The successful functionalization was demonstrated by an XPS analysis (Fig. 4) which revealed that a new *sp*³ C—C covalent bond between CALNN linker and Tf was formed while the *sp*² C=C double bonds from Tf and the C—N bond from both CALNN and Tf disappeared. This reaction may take place due to the super-electrophilic ability of CALLN that enables the formation of a transient bond with the aromatic rings of Tf (phenylalanine or histidine), resulting in the activation of the β-protons and the cleavage of the C—N bond and ammonia dissipation. This reaction is likely initiated by Friedel–Crafts attachment and is widely reported in the literature.³⁵ Furthermore, a decrease in the Z-potential of Au/AgICSD suggests the anchoring of targeted Tf molecules

on the surface of Au/AgICSD. The Z-potential changed from 23 mV for PEG-*b*-AGE coated Au/AgICSD with $-\text{NH}_2$ groups on the surface to -35 mV for Tf-Au/AgICSD after grafting transferrin on the surface (Fig. 4, bottom right panel). Furthermore, the developed PEG-*b*-AGE coated Au/AgICSD has a good biocompatibility without significant cytotoxicity up to a Au concentration of $50 \mu\text{g/ml}$.

Our results on CT contrast enhancement showed that Au/AgICSD are 4.3 times more efficient than the simple AuNPs and 3 times more efficient than the clinically used Omnipaque™ contrast agent. Even at low concentrations of gold (0.5×10^3 nM—79.8 HU), the Au/AgICSD generate satisfactory contrast in CT images. Interestingly, the AgI shell generated substantially stronger CT contrast than the AuNP core, suggesting that the loading of iodine in the shell of gold nanoparticles is a very effective and efficient way to increase the contrast effect. Similarly, the photoacoustic signal from Au/AgICSD was also much higher than that from AuNPs at the same concentration. Additionally, the HU and PAT intensity from Au/AgICSD were also much higher than those reported in the early report¹⁰ even when concentration of Au/AgICSD used in this study was 10 times lower. Therefore, the Au-AgI core/shell structure may provide some form of synergistic effect that enables further enhancement of both CT and PAI contrast, although the phenomena of this synergistic effect need to be further investigated in the future.

5. CONCLUSIONS

We report the development of a new class of core/shell dimers (Au/AgICSD) as CT/PAI dual-modal biomarker targeted contrast agents. The nanodimers are composed by uniformly fusing gold, silver, and iodine to form core-shell nanocomposite structure. TEM, STEM, XPS, and ICP-MS were used to characterize the nanodimers and confirm the core-shell formation with an overall size of 35 nm with a 15 nm AuNP core covered by a AgI shell of 5 nm. The composition ratio between these three components was determined to be 38% gold, 54.26% iodine, and 6.97% silver by ICP-MS.

The Au/AgICSD was stabilized in water by applying an amphiphilic PEG-*b*-AGE polymer coating. Surface functionalized with CALNN peptide linker allows for conjugating cell targeting ligands, e.g., transferrin. The evaluation of CT and PAI contrast enhancement demonstrated that prepared AgI/Au CSD has dual-modality contrast-enhancing capability. The Au/AgICSD is 4.3 times more efficient in CT enhancement than the AuNPs without the shell and 3 times more efficient than the clinically used Omnipaque™ 350 contrast agent. The presence of the AgI shell around the AuNP core likely provides additional contrast-enhancing effect in CT. Similarly, in PAT imaging, the optical absorption contrast is further increased with the Au/AgICSD nanodimer with the presence of the AgI shell.

ACKNOWLEDGMENTS

This work is supported in parts by NIH No. R01CA154846-02 (H.M. and L.Y.), NCI's Cancer Nanotechnology Platform

Project (CNPP) grant (No. U01CA151810-02 to H.M. and L.Y.), Emory Molecular Translational Imaging Center of NCI's *in vivo* Cellular and Molecular Imaging Center grant (ICMIC, No. P50CA128301-01A10003 to H.M. and L.Y.), and a grant from the Telemedicine and Advanced Technology Research Center (TATRC) at the U.S. Army Medical Research and Materiel Command (USAMRMC, No. W81XWH-12-1-0138 to X.T.). The authors thank Dr. Jin Xie of Department of Chemistry at University of Georgia for helping ICP-MS measurement.

- ^{a)}Authors to whom correspondence should be addressed. Electronic addresses: hmiao@emory.edu; Telephone: (404) 712-0357; Fax: (404) 712-5689 and Xiangyang.Tang@emory.edu; Telephone: (404) 712-0357; Fax: (404) 712-5689.
- ¹C. P. Karger, P. Hipp, M. Henze, G. Echner, A. Hoss, L. Schad, and G. H. Hartmann, "Stereotactic imaging for radiotherapy: Accuracy of CT, MRI, PET and SPECT," *Phys. Med. Biol.* **48**(2), 211–221 (2003).
 - ²V. Ntziachristos, "Going deeper than microscopy: The optical imaging frontier in biology," *Nat. Methods* **7**(8), 603–614 (2010).
 - ³D. J. Naczynski, M. C. Tan, R. E. Riman, and P. V. Moghe, "Rare earth nanopores for functional biomolecular imaging and theranostics," *J. Mater. Chem. B* **2**(20), 2958–2973 (2014).
 - ⁴J. Kim, Y. Piao, and T. Hyeon, "Multifunctional nanostructured materials for multimodal imaging, and simultaneous imaging and therapy," *Chem. Soc. Rev.* **38**(2), 372–390 (2009).
 - ⁵Y. Lin, H. Gao, D. Thayer, A. L. Luk, and G. Gulsen, "Photo-magnetic imaging: Resolving optical contrast at MRI resolution," *Phys. Med. Biol.* **58**(11), 3551–3562 (2013).
 - ⁶M. S. Judenhofer, H. F. Wehrl, D. F. Newport, C. Catana, S. B. Siegel, M. Becker, A. Thielscher, M. Kneilling, M. P. Lichy, M. Eichner, K. Klingel, G. Reischl, S. Widmaier, M. Rocken, R. E. Nutt, H. J. Machulla, K. Uludag, S. R. Cherry, C. D. Claussen, and B. J. Pichler, "Simultaneous PET-MRI: A new approach for functional and morphological imaging," *Nat. Med.* **14**(4), 459–465 (2008).
 - ⁷M. P. Melancon, Y. Wang, X. Wen, J. A. Bankson, L. C. Stephens, S. Jasser, J. G. Gelovani, J. N. Myers, and C. Li, "Development of a macromolecular dual-modality MR-optical imaging for sentinel lymph node mapping," *Invest. Radiol.* **42**(8), 569–578 (2007).
 - ⁸L. Sampath, S. Kwon, S. Ke, W. Wang, R. Schiff, M. E. Mawad, and E. M. Sevick-Muraca, "Dual-labeled trastuzumab-based imaging agent for the detection of human epidermal growth factor receptor 2 overexpression in breast cancer," *J. Nucl. Med.* **48**(9), 1501–1510 (2007).
 - ⁹J. Zhu, Y. Lu, Y. Li, J. Jiang, L. Cheng, Z. Liu, L. Guo, Y. Pan, and H. Gu, "Synthesis of Au-Fe₃O₄ heterostructured nanoparticles for *in vivo* computed tomography and magnetic resonance dual model imaging," *Nanoscale* **6**(1), 199–202 (2014).
 - ¹⁰Y. Jin, Y. Li, X. Ma, Z. Zha, L. Shi, J. Tian, and Z. Dai, "Encapsulating tantalum oxide into polypyrrole nanoparticles for x-ray CT/photoacoustic bimodal imaging-guided photothermal ablation of cancer," *Biomaterials* **35**(22), 5795–5804 (2014).
 - ¹¹Y. Shao, S. R. Cherry, K. Farahani, K. Meadors, S. Siegel, R. W. Silverman, and P. K. Marsden, "Simultaneous PET and MR imaging," *Phys. Med. Biol.* **42**(10), 1965–1970 (1997).
 - ¹²Y. Seo, C. Mari, and B. H. Hasegawa, "Technological development and advances in single-photon emission computed tomography/computed tomography," *Semin. Nucl. Med.* **38**(3), 177–198 (2008).
 - ¹³E. Yang, W. Qian, Z. Cao, L. Wang, E. N. Bozeman, C. Ward, B. Yang, P. Selvaraj, M. Lipowska, Y. A. Wang, H. Mao, and L. Yang, "Theranostic nanoparticles carrying doxorubicin attenuate targeting ligand specific antibody responses following systemic delivery," *Theranostics* **5**(1), 43–61 (2015).
 - ¹⁴L. C. Gontard, A. Fernandez, R. E. Dunin-Borkowski, T. Kasama, S. Lozano-Perez, and S. Lucas, "Transmission electron microscopy of unstained hybrid Au nanoparticles capped with PPAA (plasma-polyallylamine): Structure and electron irradiation effects," *Micron* **67**, 1–9 (2014).
 - ¹⁵W. Gao, W. Cao, H. Zhang, P. Li, K. Xu, and B. Tang, "Targeting lysosomal membrane permeabilization to induce and image apoptosis in cancer cells

- by multifunctional Au-ZnO hybrid nanoparticles,” *Chem. Commun. (Cambridge, U. K.)* **50**(60), 8117–8120 (2014).
- ¹⁶S. Zhang, M. Gong, D. Zhang, H. Yang, F. Gao, and L. Zou, “Thiol-PEG-carboxyl-stabilized Fe₂O₃/Au nanoparticles targeted to CD105: Synthesis, characterization and application in MR imaging of tumor angiogenesis,” *Eur. J. Radiol.* **83**(7), 1190–1198 (2014).
- ¹⁷J. Chen, Z. Guo, H. B. Wang, M. Gong, X. K. Kong, P. Xia, and Q. W. Chen, “Multifunctional Fe₂O₄@C@Ag hybrid nanoparticles as dual modal imaging probes and near-infrared light-responsive drug delivery platform,” *Biomaterials* **34**(2), 571–581 (2013).
- ¹⁸D. Gao, P. Zhang, C. Liu, C. Chen, G. Gao, Y. Wu, Z. Sheng, L. Song, and L. Cai, “Compact chelator-free Ni-integrated CuS nanoparticles with tunable near-infrared absorption and enhanced relaxivity for *in vivo* dual-modal photoacoustic/MR imaging,” *Nanoscale* **7**(42), 17631–17636 (2015).
- ¹⁹Z. Liu, T. Lammers, J. Ehling, S. Fokong, J. Bornemann, F. Kiessling, and J. Gatzjens, “Iron oxide nanoparticle-containing microbubble composites as contrast agents for MR and ultrasound dual-modality imaging,” *Biomaterials* **32**(26), 6155–6163 (2011).
- ²⁰Z. Liu, F. Pu, J. Liu, L. Jiang, Q. Yuan, Z. Li, J. Ren, and X. Qu, “PEGylated hybrid ytterbia nanoparticles as high-performance diagnostic probes for *in vivo* magnetic resonance and x-ray computed tomography imaging with low systemic toxicity,” *Nanoscale* **5**(10), 4252–4261 (2013).
- ²¹L. Cheng, J. Liu, X. Gu, H. Gong, X. Shi, T. Liu, C. Wang, X. Wang, G. Liu, H. Xing, W. Bu, B. Sun, and Z. Liu, “PEGylated WS₂ nanosheets as a multifunctional theranostic agent for *in vivo* dual-modal CT/photoacoustic imaging guided photothermal therapy,” *Adv. Mater.* **26**(12), 1886–1893 (2014).
- ²²G. Tian, X. Zhang, X. Zheng, W. Yin, L. Ruan, X. Liu, L. Zhou, L. Yan, S. Li, Z. Gu, and Y. Zhao, “Multifunctional Rb_x WO₃ nanorods for simultaneous combined chemo-photothermal therapy and photoacoustic/CT imaging,” *Small* **10**(20), 4160–4170 (2014).
- ²³X. Zheng, J. Shi, Y. Bu, G. Tian, X. Zhang, W. Yin, B. Gao, Z. Yang, Z. Hu, X. Liu, L. Yan, Z. Gu, and Y. Zhao, “Silica-coated bismuth sulfide nanorods as multimodal contrast agents for a non-invasive visualization of the gastrointestinal tract,” *Nanoscale* **7**(29), 12581–12591 (2015).
- ²⁴See supplementary material at <http://dx.doi.org/10.1118/1.4939062> for more investigations of A-D *in vitro* toxicity on cell lines at different concentrations of AuNPs and AgI/AuCSD.
- ²⁵Y. Li, R. Lin, L. Wang, J. Huang, H. Wu, G. Cheng, Z. Zhou, T. MacDonald, L. Yang, and H. Mao, “PEG-*b*-AGE polymer coated magnetic nanoparticle probes with facile functionalization and anti-fouling properties for reducing non-specific uptake and improving biomarker targeting,” *J. Mater. Chem. B Mater. Biol. Med.* **3**(17), 3591–3603 (2015).
- ²⁶P. H. Yang, X. Sun, J. F. Chiu, H. Sun, and Q. Y. He, “Transferrin-mediated gold nanoparticle cellular uptake,” *Bioconjugate Chem.* **16**(3), 494–506 (2005).
- ²⁷C. Freese, C. Uboldi, M. I. Gibson, R. E. Unger, B. B. Weksler, I. A. Romero, P.-O. Couraud, and C. J. Kirkpatrick, “Uptake and cytotoxicity of citrate-coated gold nanospheres: Comparative studies on human endothelial and epithelial cells,” *Part. Fibre Toxicol.* **9**(23), 1–11 (2012).
- ²⁸W. Cheng, S. Dong, and E. Wang, “Iodine-induced gold-nanoparticle fusion/fragmentation/aggregation and iodine-linked nanostructured assemblies on a glass substrate,” *Angew. Chem., Int. Ed. Engl.* **42**(4), 449–452 (2003).
- ²⁹A. N. Shipway, E. Katz, and I. Willner, “Nanoparticle arrays on surfaces for electronic, optical, and sensor applications,” *ChemPhysChem* **1**(1), 18–52 (2000).
- ³⁰A. N. Shipway, M. Lahav, R. Gabai, and I. Willner, “Investigations into the electrostatically induced aggregation of Au nanoparticles,” *Langmuir* **16**(23), 8789–8795 (2000).
- ³¹J. Leiro, E. Minni, and E. Suoninen, “Study of plasmon structure in XPS spectra of silver and gold,” *J. Phys. F: Met. Phys.* **13**(1), 215–221 (1983).
- ³²S. K. Jo and J. M. White, “Characterization of adsorption states of atomic iodine on Pt(111),” *Surf. Sci.* **261**(1–3), 111–117 (1992).
- ³³I. Fratoddi, I. Venditti, C. Battocchio, G. Polzonetti, C. Cametti, and M. V. Russo, “Core shell hybrids based on noble metal nanoparticles and conjugated polymers: Synthesis and characterization,” *Nanoscale Res. Lett.* **6**(1), 98 (2011).
- ³⁴M.-C. Bourg, A. Badia, and R. B. Lennox, “Gold–sulfur bonding in 2D and 3D self-assembled monolayers: XPS characterization,” *J. Phys. Chem. B* **104**(28), 6562–6567 (2000).
- ³⁵C. Paizs, A. Katona, and J. Retey, “The interaction of heteroaryl-acrylates and alanines with phenylalanine ammonia-lyase from parsley,” *Chem.–Eur. J.* **12**(10), 2739–2744 (2006).